First neutralization experiments and simulations on the CRAFT negative ion source neutral beam injection test facility[*]

Bin Li,[1,2] Jiang-Long Wei,[1,†] Wei Yi,[1] Li-Zhen Liang,[1] Yong-Jian Xu,[1]
Wei Liu,[1] Yu-Wen Yang,[1,2] Hui-Hui Hong,[1,2] and Yuan-Lai Xie[1,‡]

[1]*Institute of Plasma Physics, Hefei Institutes of Physical Science, Chinese Academy of Sciences, Hefei 230031, China*
[2]*University of Science and Technology of China, Hefei 230026, China*

A negative ion source neutral beam injection (NNBI) test facility is under construction in the Chinese large research infrastructure that the Comprehensive Research Facility for Fusion Technology (CRAFT). The CRAFT NNBI test facility aims to explore and master the key technologies of the external heating neutral beam system for future large-scale fusion reactors. Converting the energic ions from the ion source into the neutral particles (i.e., neutralization) is a key process for a NBI system, which can determine the final injection power. The first neutralization experiments on the CRAFT NNBI test facility were carried out via a dual-driver negative ion source. The beam energy was 120~170 keV and the negative ion beam current was 7~13 A (118~220 A/m^2). With the proper gas feeding into the neutralizer, the neutralization efficiency of around 60% could be achieved. For design and analysis of the whole process of beam transmission inside the beamline, a Monte-Carlo based model was built which can simulate the beam particles launch, beam particles motion, rarefied gas flow, beam-gas interaction. The model was used to analyze these first neutralization experiments, and the simulated and experimental results showed a good agreement.

Keywords: Neutral beam injection, Negative ion source, Monte Carlo method, Gas neutralization

I. INTRODUCTION

Neutral beam injection (NBI) is a principal method of auxiliary heating and current drive for kinds of magnetic confinement fusion devices [1–13]. The powerful deuterium (or its isotopes) neutrals are injected into the device and transfer their energies and momentums to the background plasma with kinds of particle collisions. For future large-scale fusion reactors, the required injecting particle energy is around 1 MeV level to attain the core plasma ignition [14–18]. At such a beam energy, the negative ion source neutral beam injection (NNBI) is more desirable due to its high neutralization efficiency rather than the positive ion source neutral beam injection (PNBI) [19]. However, the developments of a NNBI system are much more challengeable, according to the experience of the only two existed NNBI systems for JT-60U tokamak [20] and for LHD heliotron [21] respectively. To master the key techniques of NNBI system, the Institute of Plasma Physics, Chinese Academy of Sciences (ASIPP) has been constructing a NNBI test facility in the framework of the Comprehensive Research Facility for Fusion Technology (CRAFT) since 2019 [22]. CRAFT is one of the national large research infrastructures in China, which aims to explore and master fusion DEMO level key technologies, to establish the method and standard for manufacturing the key material, components and system for the China Fusion Engineering Test Reactor (CFETR) and its evolution that China Fusion Engineering DEMO Reactor (CFEDR) [23].

The neutralization of accelerated ion beam is a necessary process to inject the energic particles across the high magnetic field of the fusion device. The initial objective of the CRAFT NNBI test facility is to generate a continuous neutral hydrogen beam with the particle energy of 200~400 keV, beam power of 2 MW and pulse duration of 100 s. And the neutralization efficiency of the CRAFT NNBI test facility is designed to be >50%. Although the plasma neutralizer [24–29] and photon neutralizer [30–34] has a higher neutralization efficiency for the energic negative ions, they are still a way off to the application on the NNBI system. For the startup stage of the CRAFT NNBI test facility, the gas neutralizer is a more realistic choice, which has been used in all existing NNBI or PNBI systems worldwide due to its simple structure and high reliability.

The common key issue of a gas neutralizer is to form the optimal gas target thickness in the reasonable neutralizer length with the minimum gas inlet. For PNBI system, a problem arose at high-energy and high-power operation that the actually needed gas inlet quantity was much more than the calculated value from the gas conductance simulation. The main reason was that the gas target thickness was lower than the expected due to the gas heating or plasma formation by the beam-gas interaction. Endless increasing the gas flow to the neutralizer is not realistic, which will increase the pressure in the grid region thus making the grids more prone to electrical breakdown. It resulted in a lower neutralization efficiency than theoretical value in several PNBI systems, when the beam energy was above 80 keV [35, 36].

For NNBI system, the heating effect inside the gas neutralizer is not that severe due to the lower beam particle density and lower cross-sections at higher beam particle energy [37]. The plasma formation here can be benefic due to its higher neutralization efficiency for negative ion beam [38, 39]. The achieved neutralization efficiency was even a little higher than the theoretical value in the NNBI systems of JT-60U and LHD. For the NNBI system of the International Thermonuclear Experimental Reactor (ITER), a rectangular gas neutral-

izer will be separated to several beam channels with a large aspect ratio which can reduce the gas conductance and consequently shorten the neutralizer [40, 41].

In this paper, the first neutralization experiments on the CRAFT NNBI test facility are described. A model of the beam particle evolution in the rarified gas has been constructed to simulate the neutralization processes and to analyze the experimental results.

II. EXPERIMENTAL LAYOUTS AND CONDITIONS

A. Neutral beam test stand of CRAFT

There are two test stands in the CRAFT NNBI test facility. One is the HONOR (Hefei Open Facility for Negative Ion Source Research) test stand focusing on the negative ion source research. The HONOR beamline vacuum vessel is shorter and equipped with several beam diagnostic systems inside. The other one is the CAN·BE (CFEDR Advance Neutral Beam Equipment) test stand for developing the whole process of neutral beam injection. The neutralization experiments can be only carried out on the CANBE test stand.

The layout of CANBE test stand is shown in Fig. 1. Except the negative ion source (IS), it is composed of the beamline vessel (BLV), neutralizer (NEU), electrostatic residual ion dump (ERID), calorimeter (CAL), cryopumps, vacuum gate valve, gas baffle and other components.

BLV is a $4\times4\times12$ m^3 rectangle containing all the beamline components, connected to the ion source and the duct liner by two gate valves. Indeed, the BLV is composed of three vessels which are connected by bolts and O-rings. The three vessels are denoted as the neutralization vessel, deflection vessel, and the calorimeter vessel with the lengths of 3.9 m, 3.64 m, and 4.61 m, respectively. In addition, there are multiple ports used for the cooling water inlet and outlet, molecular pump interface, and connection of diagnostics and power supply signals [42].

The major structure of NEU is two narrow channels for the beam-gas interaction. The channels with large aspect ratio are better to reduce the gas conductance, so which can decrease the gas intake quantity or shorten the channel length. But the middle separating plate may suffer large heat load from both sides. The electron dumps are installed in front of the NEU to avoid the stray electrons from negative ion source impacting on the cryopumps directly. The length of the NEU channels is 3 m. Several gas intakes arranging in vertical direction are positioned in the middle of either NEU channel (1.5 m downstream the entrance). The height and width of the NEU channels can be changed according to the cross section of the ion beam, and the maximal opening of the NEU is 1.7×0.64 m^2 [43–45]. The distance from the entrance of NEU to the front inner wall of BLV is 0.7 m. The ample space on both sides of the neutralizer, particularly upstream, allows the cryopump to effectively absorb the additional gas emitted from the neutralizer.

The ERID is placed 0.33 m downstream the NEU exit to remove the residual fast ions by the electric field. Three standing plates are used to form two beam channels and the cross section of either channel is fixed on 0.33×2 m^2. The middle plate is insulated against the other components and is applied a positive high voltage (several kV), and the two lateral plates are on the ground potential. Under such electric fields, the middle plate will collect the negative ions and the lateral plates collect the positive ions. Indeed, the ERID here is jointed by two identical modules to reduce the applying voltage in the initial operation, either of which is 1.5 m in length. The two modules can be used independently [46].

The CAL is a V-shaped structure consisting of two panels with an opening angle of 15° and is located 1.1 m downstream the ERID. Its height is also 2 m. Each panel contains 66 groups of horizontal circular tubes and a swirl tape is embedded inside each tube to enhance the heat exchange. In addition, those horizontal tubes are interlaced and overlapped upstream and downstream. Such a structure can effectively avoid the beam particles shining through the CAL [47, 48].

Two cryopumps (cryosorption type) are installed on the two lateral walls of the BLV to maintain a high vacuum condition. The required static and dynamic pressures are at the order of 10^{-5} Pa and 10^{-3} Pa, respectively. Each cryopump is designed to be assembled with 8 identical cryogenic modules (1 m in width and 2.4 m in height for each). The cryogenic pipes among different modules are connected in series or in parallel [49, 50]. However, due to the supplier's problem, one complete cryopump and one 1/4 sized cryopump (i.e., 2 cryogenic modules) are used in the first neutralization experiments.

Considering the reduced pumping performance by using one downsizing cryopump, a gas baffle is placed in front of ERID to block the gas flow to the reflection region. The ERID was peculiarly prone to high-voltage breakdown during the commissioning of the CANBE test stand; at that time, only the 1/4 sized cryopump was used [22].

B. Dual-driver RF negative ion source

The first neutralization experiments were based on the CRAFT dual-driver RF negative ion source, as shown in Fig. 2. The source contains a RF driven negative ion generator and a single-stage negative ion accelerator [51, 52]. The negative ion generator is composed of two identical RF drivers and an expansion chamber. The RF driver consists of a ceramic discharge tube, a Faraday shield, an external RF coil of 6-turn, and a back plate. Its discharge space is 0.175 m in height of and 0.24 m in diameter. The expansion chamber has a cross section of 0.846×0.45 m^2 and the depth is 0.205 m. Four rows of magnets with a checkerboard-arrangement are installed around the lateral walls of expansion chamber to confine the plasma. The Cs vapor for enhancing the negative ion production is injected from both top and bottom walls of the expansion chamber [53]. A bias voltage plate is mounted near the ion extraction region to reduce the co-extracted electrons [54].

The negative ion accelerator comprises the grid electrode system and the relevant grid supporting frames and insula-
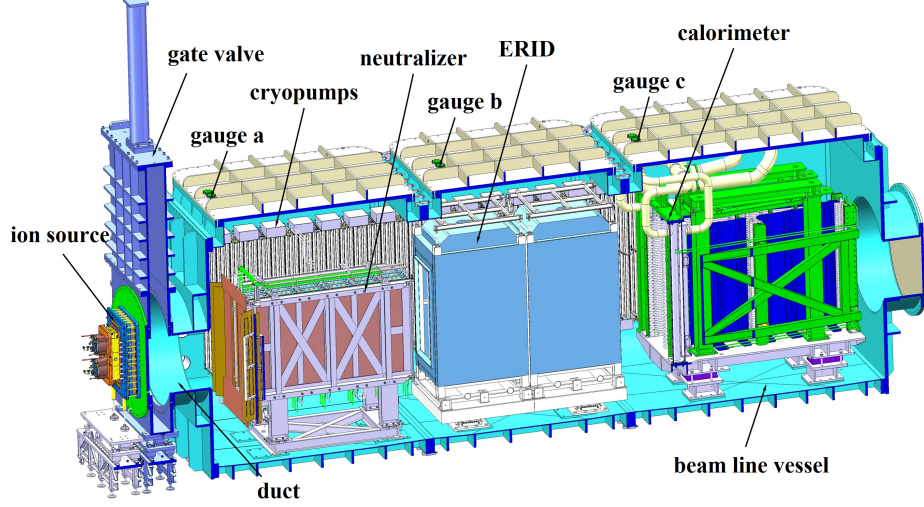
Fig. 1. (Color online) 3D structure diagram of the CANBE test stand in the CRAFT NNBI test facility.
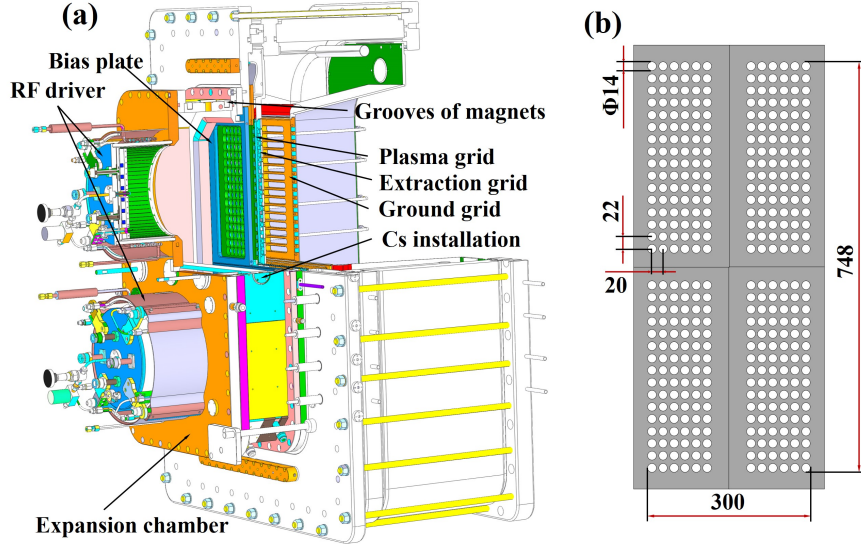

Fig. 2. (Color online) (a) 3D structure diagram of the CRAFT dual-driver RF negative ion source; (b) Aperture arrangement on the grid electrodes.

tors. There are three grid electrodes which are a plasma grid (PG), extraction grid (EG) and ground grid (GG). The extraction voltage is applied between the PG and EG for negative ion extraction (~8 kV) and the acceleration voltage is held between the EG and GG for negative ion acceleration (up to 200 kV). The thickness of PG, EG and GG are 9 mm, 17 mm and 17 mm, respectively. The gap between PG and EG is 7 mm and gap between EG and GG is 90 mm. All the three grids are composed of two segments and each segment is divided into two aperture groups. The PG and EG are multi-hole grids, but the GG is multi-slot grid which can increase the gas pumping through the GG and decrease the power load on the GG caused by stray particles [55]. Either aperture group has 16×6 apertures and the diameter of PG aperture is 14 mm.

Thus, the whole beam is composed of 384 beamlets. The distance between the centers of the two apertures is 22 mm and 20 mm on the long and short sides respectively. The total beam extraction opening is 0.748×0.3 m^2 with an effective area of 0.059 m^2 (i.e., transparency ~26.3%).

III.   MODEL DESCRIPTION

A.   Neutralization theoretical analysis

The transmission process of the negative ion beam is characterized by three particle states (H^-, H_0, H^+) and corresponding six charge transfer collisions. The cross section of each

collision varies with the particle energy [56], as shown in Fig. 3. Above $100\,\mathrm{keV}$, the dominated collisions are $H^-\to H_0$, $H_0\to H^+$, $H^-\to H^+$. According to the conservation law of matter, the variation of the ratio of different particles in the beam with the gas target thickness (i.e., the line integral of gas density $x = \int ndl$) can be described by differential Eq. (1) [57].

$$
\begin{cases}
\dfrac{dy_0}{dx} = -(C_{01} + C_{0-1})y_0 + C_{10}y_1 + C_{-10}y_{-1} \\[2mm]
\dfrac{dy_1}{dx} = -(C_{10} + C_{1-1})y_1 + C_{01}y_0 + C_{-11}y_{-1} \\[2mm]
y_{-1} = 1 - y_0 - y_1
\end{cases}
\tag{1}
$$

where C_{ij} represents the cross section of the collision $H^i \to H^j$, and y_i represents the ratio of H^i particle (i,j=+1,0,-1). The negative term signifies particle loss and the positive term represents particle generation in the equation.
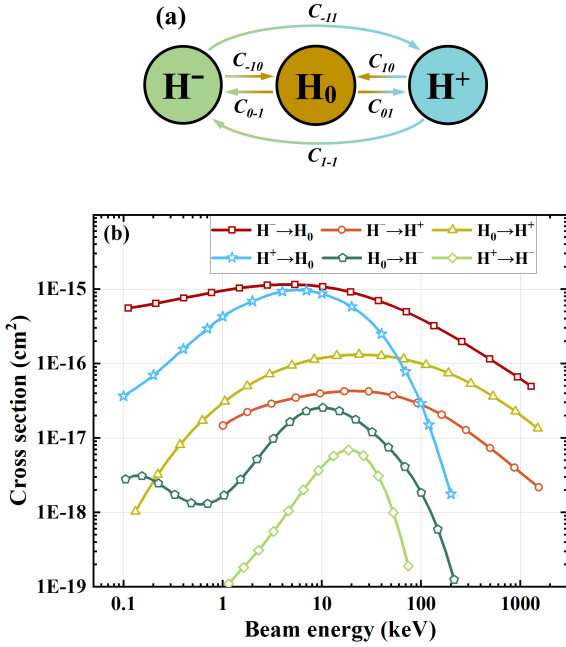

Fig. 3. (Color online) (a) Transfer of charge state of beam particles during the beam transmission. (b) Cross section of the beam particle changing collision.

By solving the Eq. (1), the fraction of H_0 and H^+ particle in the beam with gas target thickness is:

$$
y_0 = \frac{-C_{-10} + \alpha_2 S_0}{\alpha_1 - \alpha_2} e^{-\alpha_1 x} + \frac{C_{-10} - \alpha_1 S_0}{\alpha_1 - \alpha_2} e^{-\alpha_2 x} + S_0
\tag{2}
$$

$$
y_1 = \frac{-C_{-11} + \alpha_2 S_1}{\alpha_1 - \alpha_2} e^{-\alpha_1 x} + \frac{C_{-11} - \alpha_1 S_1}{\alpha_1 - \alpha_2} e^{-\alpha_2 x} + S_1
\tag{3}
$$

where

$$
S_0 = \frac{C_{10}C_{-10} + C_{1-1}C_{-10} + C_{-11}C_{10}}{\alpha_1 \alpha_2}
\tag{4}
$$

$$
S_1 = \frac{C_{01}C_{-11} + C_{0-1}C_{-11} + C_{-10}C_{01}}{\alpha_1 \alpha_2}
\tag{5}
$$

α_1 and α_2 are roots of the following Eq. (6):

$$
x^2 - \sum_{i=-1}^{1} C_{ij}x + (C_{01} + C_{0-1} + C_{-10})(C_{10} + C_{1-1} + C_{-11})
$$
$$
= (C_{01} - C_{-11})(C_{10} - C_{-10}), \quad j = -1, 0, 1 \,\&\, j \neq i
\tag{6}
$$

Plot y_i as shown in Fig. 4(a). As the increases of gas target thickness, the fraction of H_0 particle rises first and then decreases, which is a convex function. The neutralization efficiency is defined as the ratio of the power of the H_0 particle to the total power of the initial ion beam, i.e., y_0. For $400\,\mathrm{keV}$ and $200\,\mathrm{keV}$ negative ion beam, the maximum neutralization efficiency is 55.4% and 56.91%, corresponding to the optimum gas target thickness of $1.16\times10^{20}\,\mathrm{m}^{-2}$ and $6.9\times10^{19}\,\mathrm{m}^{-2}$, respectively.

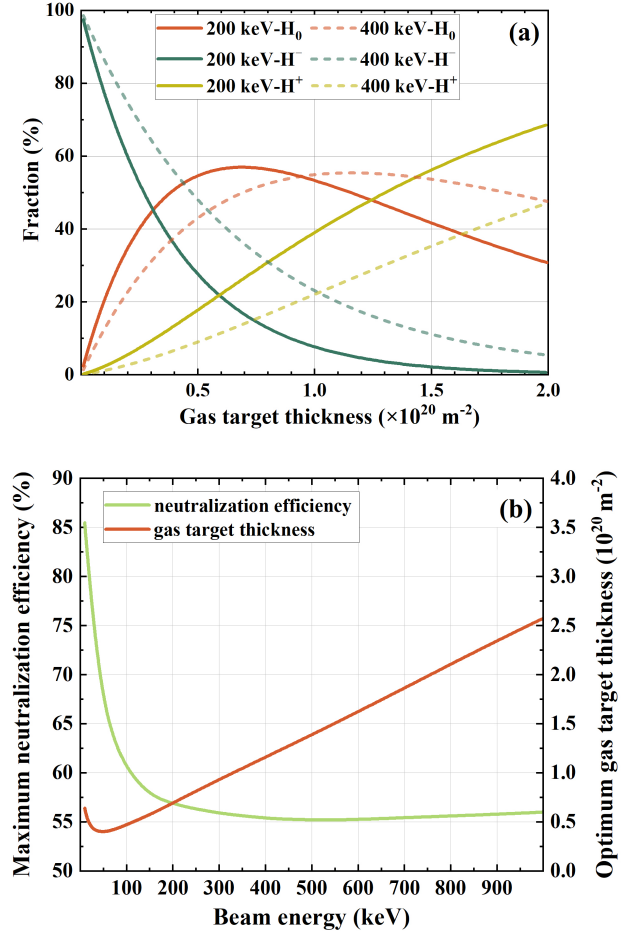Fig. 4. (Color online) (a) Evolution of the fraction of different beam particle within the different gas target thickness (e.g., $400\,\mathrm{keV}$ and $200\,\mathrm{keV}$); (b) Maximum neutralization efficiency and optimal gas target thickness of negative ion beam with beam energy.

At different beam energies, there is always a maximum

value of y_0, which is the maximum neutralization efficiency of the negative ion beam, and the corresponding x_0 is the optimal gas target thickness for neutralization. The values are:

$$y_{0 \max} = \frac{-C_{-10} + \alpha_2 S_0}{\alpha_1 - \alpha_2} Q^{\frac{\alpha_1}{\alpha_2 - \alpha_1}} +$$
$$\frac{C_{-10} - \alpha_1 S_0}{\alpha_1 - \alpha_2} Q^{\frac{\alpha_2}{\alpha_2 - \alpha_1}} + S_0 \tag{7}$$

$$x_0 = \frac{\ln Q}{\alpha_1 - \alpha_2} \tag{8}$$

where

$$Q = \frac{S_0 \alpha_1 \alpha_2 - C_{-10} \alpha_1}{S_0 \alpha_1 \alpha_2 - C_{-10} \alpha_2} \tag{9}$$

The maximum neutralization efficiency and the optimum gas target thickness at different beam energy are shown in Fig. 4(b). The maximum neutralization efficiency decreases sharply with increasing beam energy at low beam energy ($<$ 100 keV) and then decreases slowly but it can maintain about 55~56%. The optimum gas target thickness decreases and then increases with increasing beam energy, and the optimum target thickness is minimum when the beam energy is around 50 keV.

B. Gas flow model

In order to simulate and analyze the beam transmission and neutralization process, a simplified geometric model was built according to the current arrangement of the CANBE test stand, as shown in Fig. 5. Note that, the interspace in the gate valve and connection duct between the negative ion source and the BLV is taken into calculation; the ground grid is supported by the nest-shape frame (shown in Fig. 2), so there is also some beam transmission space.
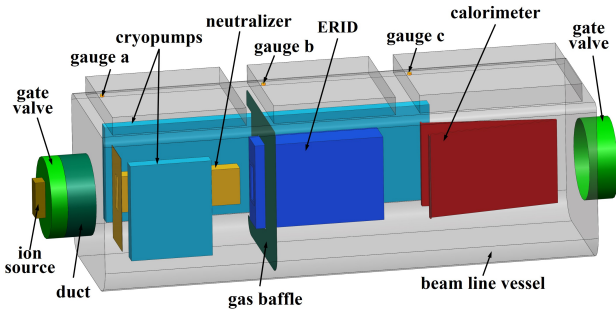

Fig. 5. (Color online) Simplified geometric model of CANBE beamline for simulation.

Based on the rarefied gas theory, the Knudsen number of the gas flow inside the BLV (i.e., the ratio of the molecular average free path λ to the characteristic length L of the gas flow) is calculated to be ~1.0 inside the neutralizer and ~100 in the rest of the BLV. This indicates that the gas flow belongs to the transitional flow regime inside the neutralizer and the molecular flow regime outside the neutralizer. According to the previous work [58], the calculated maximal gas density and gas density gradient near the gas intakes (~17% of neutralizer area) based on the transitional flow regime is smaller than that based on the molecular flow regime; In the other area of neutralizer, the gas density distribution are less different between the calculations of the transitional flow and the molecular flow.

For simplicity, the gas flow inside the whole BLV space is assumed to be in the molecular flow regime here. Thus, the collisions between the gas molecules can be ignored; the gas flow is dominated by the collisions of the gas molecules with the walls. The gas molecules exchange momentum and energy with the walls during the collisions, and the speeds of the reflected gas molecules follow the Boltzmann-Maxwell distribution and the angles follow Knudsen's cosine law. If the initial temperature of a gas molecule is T_{in} and the temperature of the wall is T_w, then the temperature of reflecting molecule is [59, 60]:

$$T_{out} = T_{in} + a(T_w - T_{in}) \tag{10}$$

where a is the thermal accommodation coefficient of the gas molecules on the wall. The a depends on the type of gas molecule, the wall temperature and the wall material. In this paper, the cryopump is simplified to an adsorption surface with 90 K. According to the previous works [40, 61], the a of the cryopump surface is 0.5 and the rest of the wall is 0.2.

The main gas sources in the whole BLV are:

1) The non-ionized gas from the ion source flows into the vessel through the grids hole with the ion beam.

2) Additional supplemental gas from the middle of neutralizer according to the beam energy.

3) The recombination of the deposited particles on the ERID panels forms the released gas determined by the neutralization efficiency η. The maximum gas flow rate is confirmed by Eq. (11) [62]:

$$Q_{ERID} = \frac{(1 - F_r)(1 - \eta)I_{ion}}{2e} \tag{11}$$

where F_r is the fraction of the reflected ions and I_{ion} represents the beam current.

4) The gas source from the calorimeter is smaller and far away from the neutralized region, so which is ignored.

The pumping speed of the cryopumps are represented by the effective capture factor c in the model, which describes the fraction of all incoming molecules which are pumped whereas the fraction $(1-c)$ is reemitted again from the cryopump. The c is determined through the calibration of pumping speed for the cryopump. The contribution of the molecular pumps is ignored.

The gas flow modeling in the BLV is based on the test particle Monte Carlo (TPMC) simulation method. The whole BLV vacuum space is divided into cells. The accumulations of flight time of the testing molecule in each cell are recorded. Then, the density in one cell is proportional to the accumulation of flight time of every molecule in this cell and inversely proportional to the cell volume [63].

C. Beam-gas interaction model

Based on the biGaussian distribution, the Monte Carlo (MC) simulation method is used to simulate the motion of beam particles. In this paper, the beamlet is considered to consists of a beam core and a beam halo with a divergence angle of 5 mrad and 30 mrad, respectively, where the beam halo accounts for 15% of the beam power [40, 43]. The collisions between the beam particles and the background gas are also calculated based on MC method. Considering that the cross sections of two types of collisions, $H^+ \rightarrow H^-$ and $H_0 \rightarrow H^-$, are relatively small compared to other types of collisions, they are not calculated in the model.

The beam particles are mainly affected by electromagnetic field force during the transmission process, and the forces is:

$$\frac{d}{dt}(m\vec{v}_p) = q\vec{E} + q\vec{v}_p \times \vec{B} \tag{12}$$

The velocity of the beam particle after the collision with the background gas particle is:

$$\vec{v}' = \vec{v}_p - \frac{m_g}{m_p + m_g}(\Delta\vec{v} - \Delta\vec{v}_d) \tag{13}$$

where,

$$\Delta\vec{v} = \vec{v}_p - \vec{v}_g \tag{14}$$

$$\Delta\vec{v}_d = \sqrt{(\Delta\vec{v})^2 - \frac{2\Delta E(m_p + m_g)}{m_p m_g}}\frac{\Delta\vec{v}}{|\Delta\vec{v}|} \tag{15}$$

m_p and m_g are the mass of the beam particle and the background particle respectively, $\vec{v}_p$ and $\vec{v}_g$ are the velocities of the beam particle and the background gas particle before the collision respectively, and ΔE is the energy loss of the collision.

IV. EXPERIMENTAL AND SIMULATION RESULTS

A. Measurement of pumping speed of cryopumps

The pumping speed of the cryopumps and the consequent gas pressure distribution is very critical to the acceleration and neutralization of negative ion beam. During the measurement of the cryopumps, (1) the gate valve between the BLV and the negative ion source was open; (2) the gate valves connecting the molecular pumps were closed; (3) both of the full-size and the 1/4-size cryopumps were used. The hydrogen gas was injected from the neutralizer and the gas flow rates Q_{in} were controlled by the mass flowmeter. The gas pressures were measured simultaneously by three vacuum gauges at different positions. As shown in Fig. 1 and Fig. 5, gauge a, gauge b and gauge c were installed through three diagnostic ports that locates at the top of the BLV and the distances from the front inner wall of BLV are 0.37 m, 4.31 m, and 7.95 m, respectively.

When the static pressure inside the BLV reached the order of 10^{-5} Pa, the gate valves connected to the molecular pump were closed. By opening the gas intakes of the neutralizer, the hydrogen gas was released into the neutralizer at a gas flow rate of 625~2500 sccm. Until the pressure was stabilized, the dynamic pressure value was recorded. The actual pumping speed of the cryopump S_p is calculated with the static pressure p_0, dynamic pressure p_d, and gas flow rate of the neutralizer Q_{in},

$$S_p = \frac{Q_{in}}{p_d - p_0} \tag{16}$$

The measured gas pressures of these three gauges are shown in Fig. 6 with different gas flow rates of the neutralizer. Commonly, there is always a gas pressure gradient from the gas source to the gas pump (also shown in Sec. IV-B), so the gas pressures are different at these three positions. A gas flow simulation was carried out with the similar conditions of the pumping speed measurement, to evaluate the effective capture factor of the cryopumps. The room-temperature gas injected from the neutralizer was the only gas source; except the cryopumps, all the surfaces were set to be the room temperature. The simulated gas pressure at the same positions of those three gauges are also shown in Fig. 6 with the different effective capture factors and different gas flow rates. In general, there is an effective capture factor where the simulated values are quite consistent with the measurements. By calculating the average error between the simulated and measured dynamic pressure in different gas flow rates (as shown in Fig. 7, error $\sigma = \sqrt{\sum(p_s - p_d)^2/n}$), where p_s is the simulated pressure, p_d is the measured dynamic pressure, n is the comparison number), the effective capture factor of the cryopumps is evaluated to be 0.33, which is quite close to the design value of 0.34.

The pumping speed of the cryopumps (one full-size and one 1/4-size cryopumps) measured by the vacuum gauges a, b and c at different gas flow rates of the neutralizer is shown in Fig. 8. As the gas flow rate of the neutralizer becomes larger, the pumping speeds measured decrease slightly, but the maximum doesn't exceed 10%, which may be caused by the lower adsorption capacity on the surface due to the larger volume of hydrogen gas.

B. Simulation of gas flow during beam operation

The typical waveforms of negative ion beam acceleration and neutralization are shown in Fig. 9, where the power of the RF driver was set to 60.0 kW and the actual operation reached 49.2 kW. The extraction and acceleration voltages were 4.6 kV and 128.0 kV, respectively; the H^- beam current was 7.0 A and the pulse duration was 20.0 s. The applied voltage on the ERID was 5.2 kV. The gas inlet rate from the negative ion source was constant to be 2000 sccm, which corresponded to the filling gas pressure of 0.4 Pa.

During the beam operation, the particle and heat flux on the beamline components can increase their surface temper-
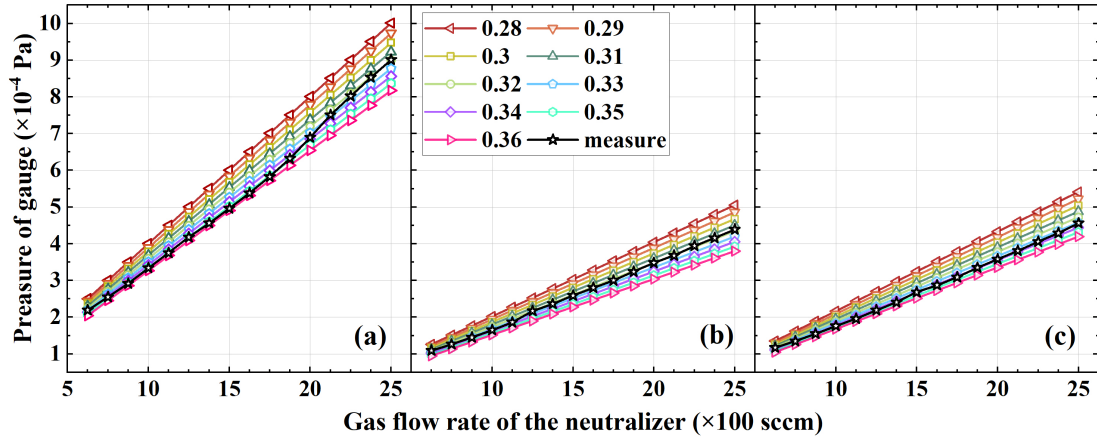
Fig. 6. (Color online) Simulated pressures at gauges a, b, and c with different effective capture factor and different gas flow rates of the neutralizer, and comparing to the measured dynamic pressures.
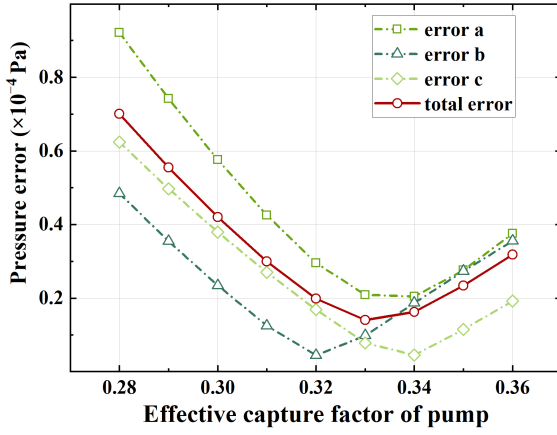

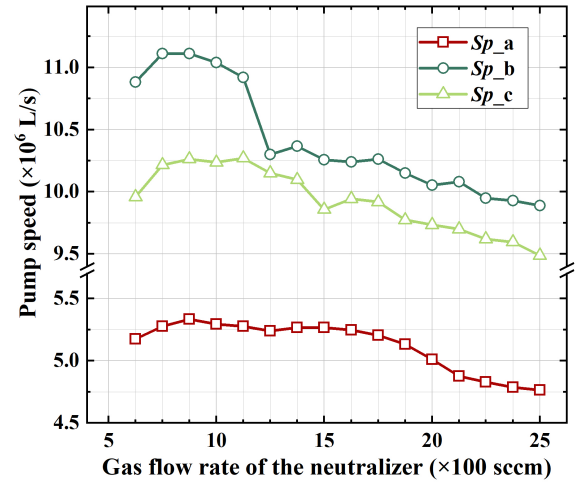Fig. 7. (Color online) Average error between measured and simulated pressure at gauges a, b, and c.

Fig. 8. (Color online) The actual pumping speed of the cryopump as a function of gas flow rate of the neutralizer.

ature. The simulated gas density distribution along the direction of beam transmission after considering the thermal accommodation on the walls is shown in Fig. 10. The gas temperature from the negative ion source was 650 K in this model [43], and the temperature on the surface of the neutralizer and the ERID were supposed to be 370 K and 420 K under the condition of sufficient cooling water [40, 46]. The main gas load (about 80~90% of the total) comes from the neutralizer, which was set to 0~6000 sccm [64]. As the additional supplemental gas to the neutralizer is increased, it not only increases the gas density inside the neutralizer, but also raises the gas pressure inside the grids gap and increases the risk of high-voltage breakdown. When the neutralizer gas flow rate reaches the maximum of 6000 sccm, the pressure at the ground grid is calculated to be about 0.03 Pa. The gas density along the direction of beam transmission shows a gradient distribution with the largest inside the neutralizer, then upstream and downstream of the neutralizer, and the smallest inside the calorimeter.

Fig. 11 shows the gas density distribution in the vertical direction to the beam transmission at the upstream and the downstream of the neutralizer and the downstream of the ERID, respectively. The maximum of the gas density is in the center of the BLV, not the beam channel. On the one hand, the gas from the two beam channels converges to form the peak density in the center of the vessel. On the other hand, the gas in the center of the beam channel diffuses in both directions toward the cryopump and the center of the BLV, resulting in a decrease in density. It decreases almost linearly in the region where the beam passes through, which is caused by the gas supply of the neutralizer and the larger the gas supply, the faster the decrease is. In the other regions, the rate of decrease is gradually flat. The curves are not completely symmetric, especially Fig. 11(c), mainly caused by asymmetric cryopumps. Due to the presence of the gas baffle in the BLV, only one side has cryopump for gas adsorption, resulting in
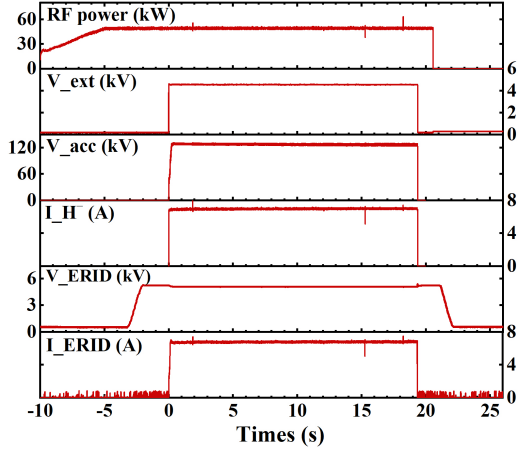
Fig. 9. (Color online) Typical waveforms of negative ion acceleration and neutralization.
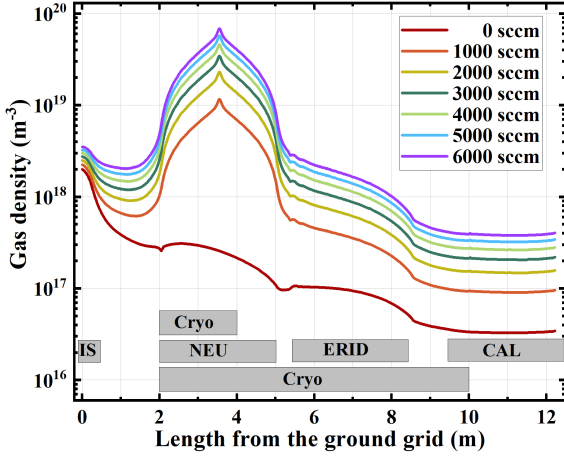

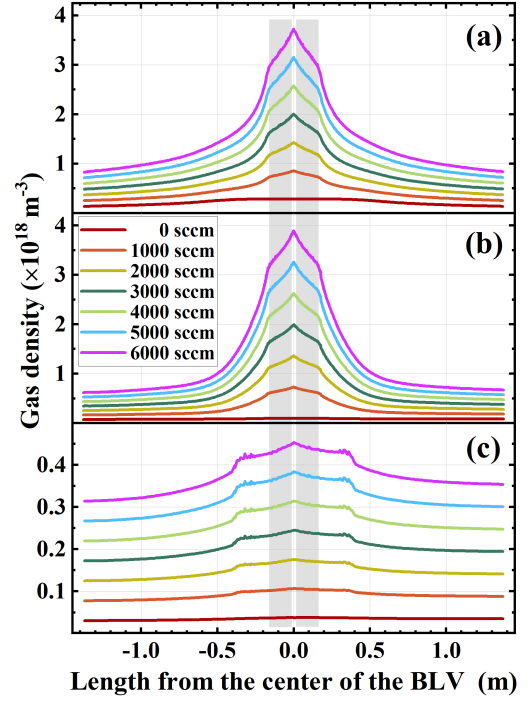Fig. 10. (Color online) Distribution of gas density along the centerline of beam transmission.

Fig. 11. (Color online) Gas density distribution in the vertical direction to the beam transmission: (a) upstream of the neutralizer; (b) downstream of the neutralizer; (c) downstream of the ERID. The gray area represents the beam channel.

the right side of the curve being slightly higher than the left, especially in the non-beam channel area. In the future, two complete cryopumps will be installed on both sides to eliminate this effect.

The gas target thickness is usually considered to be the sum of the gas densities at the center of the beam channel through the neutralization vessel. Fig. 12 shows the gas target thickness at various locations in the beam channel, and the coordinate (r, s) indicates the location where the thickness was calculated, where r is the height from the center of the neutralizer ($r > 0$ indicates near the top of the BLV) and q is the width from the center of the neutralizer ($q > 0$ indicates the beam channel near the 1/4 sized cryopump). The center plane is close to the gas intakes of the neutralizer, so the gas target thickness is higher near the middle plate of the neutralizer and gradually decreases toward the lateral plates until it becomes flat. It is basically symmetric of gas target thickness throughout the beam channel, but with a slight deviation whose maximum does not exceed 0.39%, as shown in Fig. 13.

It can be assumed that gas target thicknesses of two channels of the neutralizer are the same.

When the gas flow rate from the ion source and the neutralizer alone, the gas target thicknesses at different gas flow rates are shown in Fig. 14(a). The gas target thickness formed by the neutralizer occupies the major portion and that formed by the ion source is insignificant. Changing the gas flow rate of the ion source has very little effect on the gas target thickness. For example, when the gas flow rate of the neutralizer is 3000 sccm, the gas target thickness generated by the neutralizer occupies exceed 90%. If the gas flow rate of the ion source rises by 500 sccm, the change in gas target thickness is only 2.13%. As the temperature of the neutralizer and ERID increases, the gas target thickness decreases as shown in Fig. 14(b), which is caused by the gas molecules moving more vigorously and the larger conductance. Increasing temperature of the neutralizer and the ERID causes the frequency to decrease by up to 0.15% K^{-1} and 0.002% K^{-1}, respectively. The ERID temperature increase has a negligible effect on gas target thickness, but the neutralizer is negligible only at low gas flow rates (< 3000 sccm).

C. Measurements of neutralization efficiency

The common measuring method of the neutralization efficiency is to measure and compare the neutral beam power
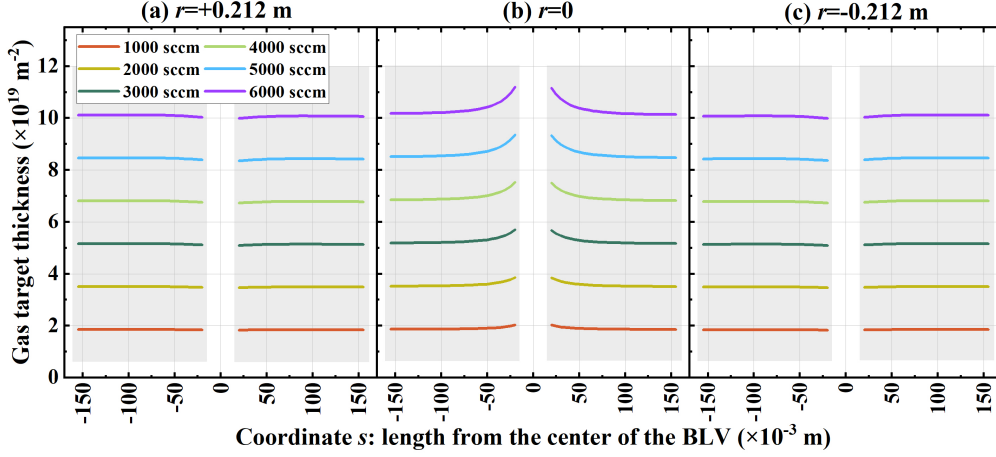
Fig. 12. (Color online) Gas target thickness at different locations of the neutralization vessel. The gray area represents the beam channel.
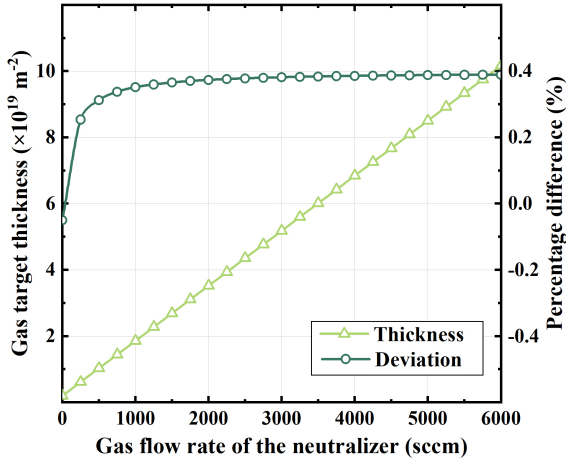

Fig. 13. (Color online) Average gas target thickness and thickness uniformity with the gas flow rate of the neutralizer.
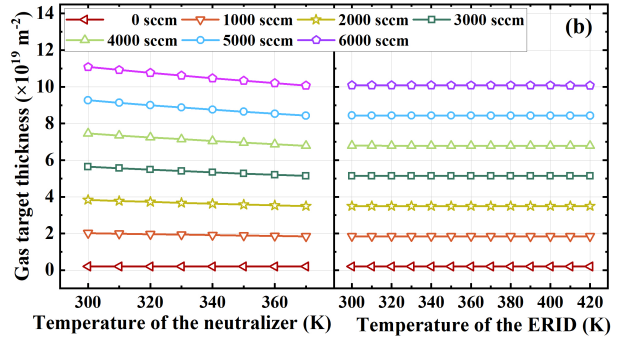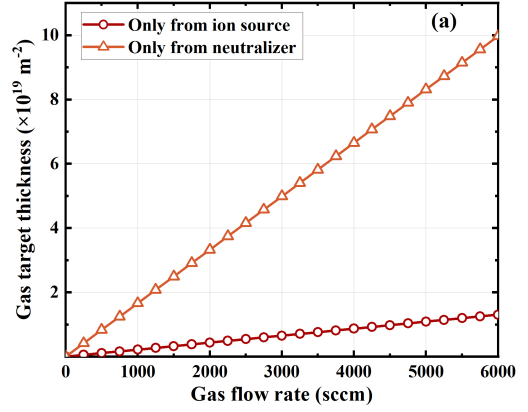

Fig. 14. (Color online) (a) Gas target thickness when gas flow rate from the ion source and the neutralizer alone. (b) Relationship between gas target thickness and component temperature.

and the mixed beam power on the calorimeter (or called beam dump) [36, 65, 66]. When the ion bending system (i.e., ERID in the CANBE test stand) is turned on, the residual ion beam downstream the neutralizer is removed from the beam channel and the calorimeter downstream is regarded as collecting the neutral beam only; conversely, when the ion bending system is turned off, the calorimeter is dumped the whole ion and neutral beam. The deposited energy on the calorimeter Q can be calculated according to the measured temperature rise of cooling water ΔT and the corresponding water flow rate m' (i.e., water flow calorimetry, WFC)

$$Q = c_p m' \int_0^\infty \Delta T(\tau)\, d\tau \qquad (17)$$

where τ is the acquisition duration. Thus, on the CANBE test stand, by comparing the deposited energy on the CAL with the similar beam parameters but with the ERID turning on and off respectively, the neutralization efficiency η can be estimated

$$\eta = \frac{Q_{CAL\ with\ ERID\ on}}{Q_{CAL\ with\ ERID\ off}} \qquad (18)$$

Before the first neutralization experiments, the dual-driver negative ion source has experienced hundreds shots of Cs conditioning and beam acceleration on the CANBE test stand. A stable negative ion beam with energy of 132 keV and current of 7 A (~118 A/m^2) can be obtained, as shown in Fig. 9.

Firstly, the experiments to measure the variation of the neutralization efficiency with the gas flow rate of the neutralizer were carried out under the same beam parameters. The gas flow rate of the negative ion source was always maintained at 2000 sccm. The gas flow of the neutralizer was controlled to vary continuously from 0~2500 sccm, and the cooling water temperature change of the flow through the calorimeter was simultaneously recorded, from which the neutralization efficiency under the experiment could be calculated (as shown in Fig. 15). The measured neutralization efficiency was raised with the increasing gas flow rate of the neutralizer, and reached a maximal value of 61% with the gas flow rate of 2000 sccm. When further increasing the gas flow rate, the neutralization efficiency tended to decline.

The simulated values of neutralization efficiency based on the calculated gas flow in Sec. IV-B are also indicated in Fig. 15(a). In calculating the neutralization efficiency using the MC method, we define the neutralization efficiency as the ratio of the energy of all neutral particles in the computational domain after the beam leaves the neutralizer to the initial ion beam energy. The maximum simulated neutralization efficiency was 57.83% at the gas flow rate of 3200 sccm. The simulated and experimental results have a similar trend, but the simulated values were lower than the experimental ones under the same gas flow rate of the neutralizer. The differences between experiments and simulation may come from:

1) The power deposited on the calorimeter (< 1 MW) is much lower than its design capacity (~10 MW). It may cause the energy calculated by WFC method had a large error to the actual value (especially for the short-pulse operation), resulting in a larger error of neutralization efficiency.

2) The contribution of plasma formation inside the neutralizer, which will increase the neutralization efficiency, is not taken into account in the MC calculation model, so the calculated neutralization efficiency may be slightly low.

3) The calorimeter still also contains some inert H^+ particles which are generated by re-ionization of the H_0 particles after the ERID. This part of the energy cannot be excluded when measuring the neutralization efficiency by using the WFC method, so the measurement point will drift upward.

The neutralization efficiency was measured for different beam energies (120~170 keV) and beam currents (7~13 A), shown in Fig. 15(b). Because the current R&D stage was still focused on the negative ion extraction and acceleration, the optimal neutralization efficiency was not pursued for each beam energy. Furthermore, there was a limitation to increase the inlet gas flow from the neutralizer (e.g., for the beam energy of ~170 keV). The electric breakdowns between the high-voltage plate and the ground-potential plates of ERID were too frequent. The application of full-size cryopump can alleviate this problem in future.

D.   Estimation of re-ionization loss

When leaving the neutralizer, the neutral beam is inevitable to be re-ionized by the collisions with the background gas, resulting in a reduction of the neutral beam power. The re-ionization loss is hard to be measured directly, which was estimated by the same model during the first neutralization experiments. Here, the re-ionization loss was defined as the ratio of the energy of vanishing neutral beam to the energy of the initial ion beam. When the beam energy is 200 keV, the beam loss due to re-ionization downstream of the neutralizer reaches 1.828%. As the gas flow rate of the neutralizer increases, the re-ionization loss of the neutral beam gradually increases with an almost proportional trend, as shown in Fig. 16. And the lower the beam energy, the more obvious the re-ionization loss.

The re-ionization loss energy consists of two parts. One part, the neutral particles are re-ionized inside the ERID, and the ionized particles are deposited on the ERID plate by the electric field force. The other part, the neutral particles are re-ionized downstream of the ERID, and the ionized particles, whose electric field force is very small or even negligible, follow the neutral beam and deposit on the calorimeter. Under the same conditions, the energy deposited on the ERID occupies the major part of the re-ionization loss energy (about 2/3). This is due to the non-negligible transmission distance of the neutral beam inside the ERID in the calculated model and the higher gas density of the background gas inside the ERID.

When the neutral beam is injected into the CRAFT or CFEDR tokamak in the future, the re-ionization loss in the duct will be more obvious than CANBE because of the longer transmission distance. Furthermore, the neutralization efficiency curve does not vary significantly with the gas flow rate of the neutralizer near the peak, as seen in Fig. 4(a). Therefore, the gas flow rate of the neutralizer can be slightly lower by 3~5% than that corresponding to the maximum neutralization efficiency in the experiment, i.e., the actual neutralization efficiency can be controlled at 95~98% of the maximum neutralization efficiency in anticipation of reducing the load of the cryopump as well as the re-ionization loss downstream of the neutralizer.

E.   Influence of beamlet divergence angle

As the quality of the initial ion beam decreases, i.e., the beamlet divergence angle increases, the transmission efficiency from the ground grid to the calorimeter subsequently decreases almost linearly due to the interception of the beam line components. When the beamlet divergence angle is less than 7 mrad, the transmission efficiency can reach more than 87.715% (shown in Fig. 17(a)).

As the beam divergence angle increases, the neutralization efficiency also decreases because the neutralizer plates will intercept a portion of the particles with large beam divergence angles. These particles stop moving without passing the neutralizer completely, and the neutralization efficiency of this part of the particles is much lower due to the lower gas thickness, so the neutralization efficiency of the entire ion beam decreases. But at least it decreases relatively slower than the transmission efficiency and the total efficiency of
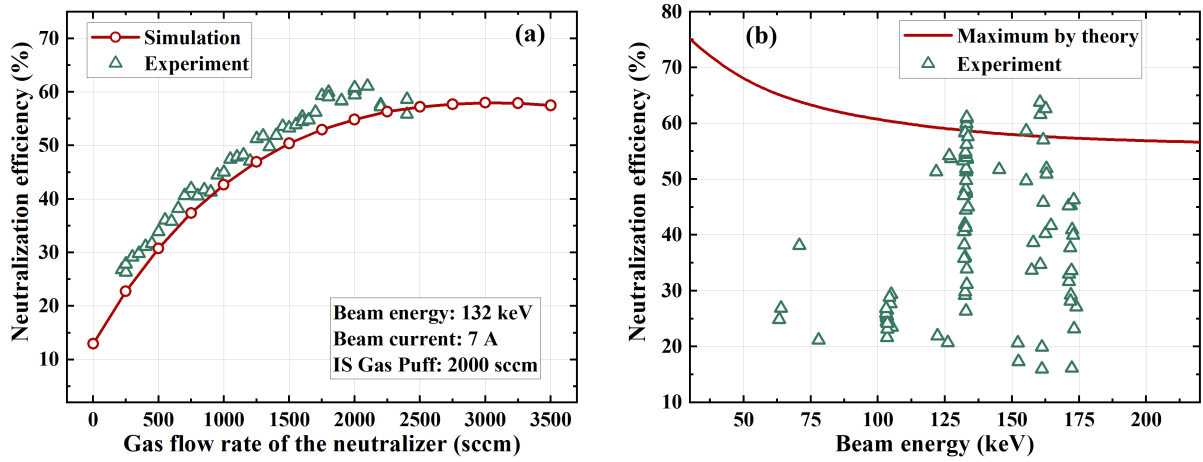
Fig. 15. (Color online) (a) Measured neutralization efficiency at different gas flow rates of the neutralizer. (b) Measured neutralization efficiency at different beam energies.
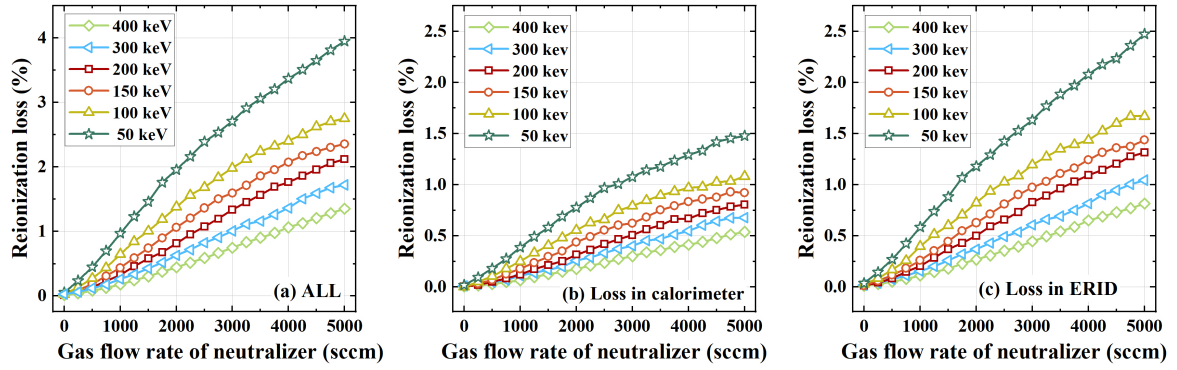

Fig. 16. (Color online) Simulated re-ionization loss at different gas flow rate of the neutralizer.(a)All re-ionization loss energy;(b)Re-ionization loss energy deposited on the calorimeter; (c) Re-ionization loss energy deposited on the ERID.
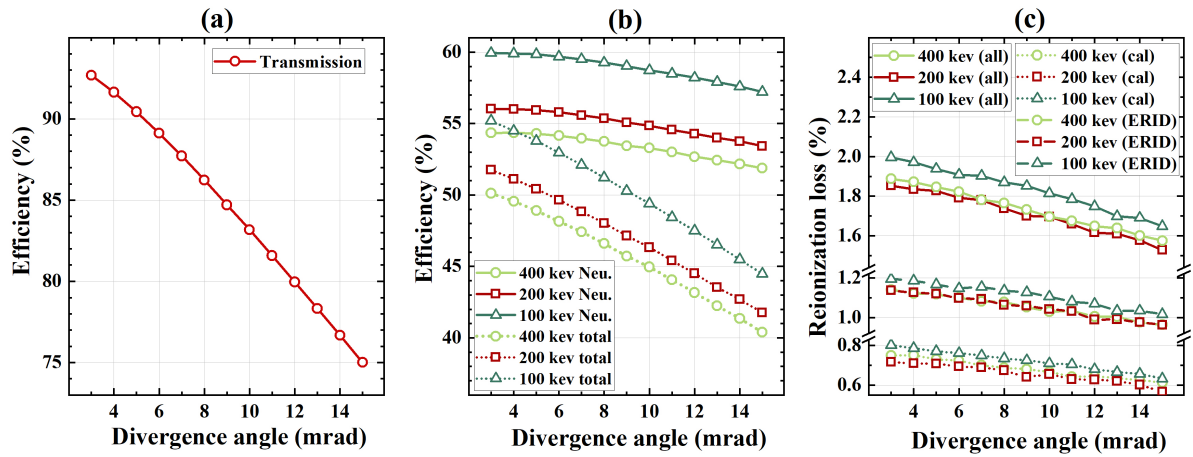

Fig. 17. (Color online) The influence of beam divergence angle. a) Transmission efficiency; b) Neutralization efficiency and total efficiency of the calorimeter; c) Re-ionization loss of the neutral beam.

[640] the calorimeter. Especially, when the beam divergence angle [641] is less than 7 mrad, the decrease of the neutralization effi- [642] ciency is very small and almost unchanged because the neu- [643] tralizer intercepts fewer particles in the beam core under this

condition, which is consistent with the design requirement of CRAFT NNBI of < 7 mrad.

On the other hand, the total efficiency of the calorimeter decreases very significantly with the increase of the beam divergence angle, and the degree of decrease is almost linear. This is mainly due to the fact that it is caused by a combination of both the neutralization efficiency and the transmission efficiency. Fig. 17 shows the trend under optimal gas flow rate. The trend of the re-ionization loss of the neutral beam is similar. As the beam divergence angle increases, the re-ionization loss decreases. The reason for this change is also due to the interception of the beam line components.

For different beam energies (200 keV or 400 keV), the two curves of neutralization efficiency versus beam divergence angle have the same trend and remain basically parallel, i.e., the magnitude of the change is independent of the beam energy. A similar situation is observed for the re-ionization loss and the total efficiency of the calorimeter.

V. CONCLUSIONS

This paper focuses on the neutralization experiment and analysis of the negative ion beams for NNBI system. The neutralization efficiency and its trend with beam energy and divergence angle were calculated based on the Monte Carlo method, and the re-ionization loss was also estimation. Neutralization efficiency was measured in the experiment based on the WFC method.

The CANBE test stand was used as a blueprint to build a negative ion beam transmission model. The relationship between the neutralization efficiency and the thickness of the background gas target was derived theoretically, and the boundary conditions required to calculate the background gas density distribution and particle collisions in the model were also given. According to the measurement of the pressure inside the beam line vessel, the pumping speed of the simplified cryopump was calibrated, and the adsorption coefficient was defined as 0.33 in the model.

The background gas density distribution of the beam line vessel at different gas flow rates of the neutralizer was described, and then the collisions of beam particles with background gas particles were calculated. For the 200 keV negative hydrogen beam, the maximum neutralization efficiency was 55.94% and the transmission efficiency was 90.44% at beam divergence angle of 5 mrad. The maximum neutralization efficiency decreased with increasing beam energy, while the re-ionization loss increased on the contrary. The larger the beam divergence angle, the lower the maximum neutralization efficiency, which was related to the decrease in transmission efficiency.

In the experiment, the neutralization efficiency of the CANBE test stand was measured by the WFC method. Under the condition of beam energy 132 keV and beam current 7 A, the maximum neutralization efficiency was measured to be about 61%, and the gas flow rate of the neutralizer was about 2000 sccm. When compared with the value calculated by the MC method, the two data are quite agreement. Furthermore, the neutralization efficiency of beam at different energies was measured partially.

[1] D.B. King, R. Sharma, C.D. Challis, et al., Tritium neutral beam injection on JET: calibration and plasma measurements of stored energy. Nucl. Fusion **63**, 112005 (2023). doi: 10.1088/1741-4326/acee97

[2] C. Hopf, N. den Harder, B. Heinemann, et al., Decoupling beam power and beam energy on ASDEX Upgrade NBI with an variable extraction gap system. Nucl. Fusion **64**, 096017 (2024). doi: 10.1088/1741-4326/ad63b9

[3] S. Ding, A.M. Garofalo, H.Q. Wang, et al., A high-density and high-confinement tokamak plasma regime for fusion energy. Nature **629**, 555-560 (2024). doi: 10.1038/s41586-024-07313-3

[4] B. Na, J. Kang, M.W. Lee, et al., Experimental and numerical evaluation of the neutral beam deposition profile in KSTAR. Fusion Eng. Des. **185**, 113320 (2022). doi: 10.1016/j.fusengdes.2022.113320

[5] Y.H. Xie, C.D. Hu, S. Liu, et al., Long pulse operation of neutral beam injector on EAST tokamak. Fusion Eng. Des. **193**, 113744 (2023). doi: 10.1016/j.fusengdes.2023.113744

[6] X.F. Yang, H.L. Wei, Y.X. Wan, et al., Study on transmission efficiency of 7 MW neutral beam injector for HL-3 tokamak. Nucl. Tech. **47**, 050011 (2024). (in Chinese) doi: 10.11889/j.0253-3219.2024.hjs.47.050011

[7] M. Hanada, A. Kojima, Y. Tanaka, et al., Progress in development and design of the neutral beam injector for JT-60SA. Fusion Eng. Des. **86**, 835-838 (2011). doi: 10.1016/j.fusengdes.2011.04.068

[8] P. Vincenzi, P. Agostinetti, R. Ambrosino, et al., Interaction of high-energy neutral beams with Divertor Tokamak Test plasma. Fusion Eng. Des. **189**, 113436 (2023). doi: 10.1016/j.fusengdes.2023.113436

[9] M.D. Boyer, S. Kaye and K. Erickson, Real-time capable modeling of neutral beam injection on NSTX-U using neural networks. Nucl. Fusion **59**, 056008 (2019). doi: 10.1088/1741-4326/ab0762

[10] J.F. Rivero-Rodríguez, K.G. McClements, M. Fitzgerald, et al., Overview of fast particle experiments in the first MAST Upgrade experimental campaigns. Nucl. Fusion **64**, 086025 (2024). doi: 10.1088/1741-4326/ad56a2

[11] R.M. Magee, K. Ogawa, T. Tajima, et al., First measurements of p^{11}B fusion in a magnetically confined plasma, Nat. Commun. **14**, 955 (2023). doi: 10.1038/s41467-023-36655-1

[12] S.A. Lazerson, O. Ford, S. Äkaslompolö, et al., First neutral beam experiments on Wendelstein 7-X. Nucl. Fusion **61**, 096008 (2021). doi: 10.1088/1741-4326/ac121c

[13] H. Gota, A. Smirnov, M.W. Binderbauer, et al., Enhanced plasma performance in C-2W advanced beam-driven field-reversed configuration experiments. Nucl. Fusion **64**, 112014 (2024). doi: 10.1088/1741-4326/ad4536

[14] A.R. Polevoi, A.A. Ivanov, S.Y. Medvedev, et al., Reassessment of steady-state operation in ITER with NBI and EC heating and current drive. Nucl. Fusion **60**, 096024 (2020). doi: 10.1088/1741-4326/aba335

[15] M.Q. Tran, P. Agostinetti, G. Aiello, et al., Status and

future development of Heating and Current Drive for the EU DEMO. Fusion Eng. Des. **180**, 113159 (2022). doi: 10.1016/j.fusengdes.2022.113159

[16] Y.t. Song, J.g. Li, Y.x. Wan, et al., Engineering design of the CFETR machine. Fusion Eng. Des. **183**, 113247 (2022). doi: 10.1016/j.fusengdes.2022.113247

[17] S. Sugiyama, N. Aiba, N. Asakura, et al., Development of pulsed plasma operation scenario and required conditions in JA DEMO. Nucl. Fusion **64**, 076014 (2024). doi: 10.1088/1741-4326/ad49b6

[18] A. Simonin, H. Bourvard and B.P. Duteil, CIGALE: an innovative gas neutralizer based high efficiency neutral beam injector concept for future fusion reactors. Nucl. Fusion **64**, 096029 (2024). doi: 10.1088/1741-4326/ad645f

[19] R.S. Hemsworth and T. Inoue, Positive and negative ion sources for magnetic fusion. IEEE Trans. Plasma Sci. **33**, 1799-1813 (2005). doi: 10.1109/Tps.2005.860090

[20] M. Kashiwagi, J. Hiratsuka, M. Ichikawa, et al, 100 s negative ion accelerations for the JT-60SA negative-ion-based neutral beam injector. Nucl. Fusion **62**, 026025 (2022). doi: 10.1088/1741-4326/ac388a

[21] K. Tsumori, K. Ikeda, M. Kisaki, et al, Challenges toward improvement of deuterium-injection power in the Large Helical Device negative-ion-based NBIs. Nucl. Fusion **62**, 056016 (2022). doi: 10.1088/1741-4326/ac2d59

[22] J.L. Wei, Y.H. Xie, Y.L. Xie, et al., Comprehensive research facility for negative ion source neutral beam injection at CRAFT: design and first operations. Plasma Sci. Technol., (2024) doi: 10.1088/2058-6272/ad8da7

[23] J.X. Zheng, J.G. Qin, K. Lu, et al., Recent progress in Chinese fusion research based on superconducting tokamak configuration. Innovation **3**, 100269 (2022). doi: 10.1016/j.xinn.2022.100269

[24] R. S. Hemsworth and P. Veltri, Design of a plasma neutraliser for a fusion reactor or as an upgrade to the ITER heating neutral beam injectors. Fusion Eng. Des. **202**, 114322 (2024). doi: 10.1016/j.fusengdes.2024.114322

[25] R.S. Hemsworth, Plasma and gas neutralisation of high energy H and D in an Argon plasma neutraliser, Fusion Eng. Des. **206**, 114578 (2024). doi: 10.1016/j.fusengdes.2024.114578

[26] A. Pimazzoni, E. Sartori and G. Serianni, On the role of dissociative recombination on the effectiveness of a plasma neutralizer in DEMO fusion plant. Fusion Eng. Des. **171**, 112693 (2021). doi: 10.1016/j.fusengdes.2021.112693

[27] G. Starnella, C. Hopf and P.N. Maya, On suitable experiments for demonstrating the feasibility of the beam-driven plasma neutraliser for neutral beam injectors for fusion reactors. Nucl. Fusion **62**, 066038 (2022). doi: 10.1088/1741-4326/ac5f18

[28] I. Turner and A.J.T. Holmes, Model for a beam driven plasma neutraliser based on ITER beam geometry, Fusion Eng. Des. **149**, 111327 (2019). doi: 10.1016/j.fusengdes.2019.111327

[29] M. Hanada, M. Kashiwagi, T. Inoue, et al., Experimental comparison between plasma and gas neutralization of high-energy negative ion beams, Rev. Sci. Instrum. **75**, 1813-1815 (2004). doi: 10.1063/1.1699462

[30] H.H. Hong, L.Z. Liang, Y.L. Xie, et al. Conceptional design of photoneutralization test system for negative ion-based neutral beam injection. Nucl. Eng. Technol., (2024). doi: 10.1016/j.net.2024.08.024

[31] S.S. Popov, M.G. Atlukhanov, A.V. Burdakov, et al., Study of the method of photon neutralization of powerful beams of negative ions at the Budker Institute of Nuclear Physics, Plasma Phys. Rep. **50**, 514-523 (2024). doi: 10.1134/S1063780x24600233

[32] A. Simonin, C. Blondel, W. Chaibi, et al., Towards a maintainable and high efficiency neutral beam system for future fusion reactors, Nucl. Fusion **61**, 046003 (2021). doi: 10.1088/1741-4326/abdac2

[33] P. Vincenzi, A. Fassina, L. Giudicotti, et al., Design and mockup tests of the RING photo-neutralizer optical cavity for DEMO NBI. Fusion Eng. Des. **146**, 1360-1363 (2019). doi: 10.1016/j.fusengdes.2019.02.076

[34] S.S. Popov, M.G. Atlukhanov, A.V. Burdakov, et al., Neutralization of negative hydrogen and deuterium ion beams using non-resonance adiabatic photon trap, Nucl. Fusion **58**, 096016 (2018). doi: 10.1088/1741-4326/aacb02

[35] B. Crowley, J. Rauch and J.T. Scoville, Modeling and experimental studies of the DIII-D neutral beam system. Fusion Eng. Des. **96-97**, 443-446 (2015). doi: 10.1016/j.fusengdes.2015.02.028

[36] E. Surrey, C.D. Challis, D. Ciric, et al. Measurement of the depletion of neutraliser target due to gas heating in the JET neutral beam injection system. Fusion Eng. Des. **73**, 141-153 (2005). doi: 10.1016/j.fusengdes.2005.06.348

[37] M. Porton and E. Surrey, Efficiency of neutral beam neutralizers in JET and ITER. Fusion Eng. Des. **86**, 797-800 (2011). doi: 10.1016/j.fusengdes.2010.11.019

[38] E. Surrey and A.J.T. Holmes, The beam driven plasma neutralizer. AIP Conf. Proc. **1515**, 532-540 (2013). doi: 10.1063/1.4792825

[39] R. McAdams, A.J.T. Holmes, D.B. King, et al, Negative ion research at the Culham Centre for Fusion Energy (CCFE). New J. Phys. **18**, 125013 (2016). doi: 10.1088/1367-2630/aa4fa1

[40] M. D. Palma, E. Sartori, W. Gonzalez, et al., Design and R&D for manufacturing the MITICA Neutraliser and Electron Dump, Fusion Eng. Des. **88**, 1020-1024 (2013). doi: 10.1016/j.fusengdes.2013.01.018

[41] R.S. Hemsworth, D. Boilson, P. Blatchford, et al., Overview of the design of the ITER heating neutral beam injectors. New J. Phys. **19**, 025005 (2017). doi: 10.1088/1367-2630/19/2/025005

[42] Q.X. Wang, Y.L. Xie, H.H. Hong, et al., Simulation and experiment of CRAFT NNBI cryopump. Fusion Eng. Des. **207**, 114637 (2024). doi: 10.1016/j.fusengdes.2024.114637

[43] Z.Y. Zhang, G.D. Wang, C.Q. Chen, et al., Physical design of the neutralizer for CFETR negative ion based neutral beam injection prototype. Fusion Eng. Des. **148**, 111316 (2019). doi: 10.1016/j.fusengdes.2019.111316

[44] J.L. Wei, Z.Y. Zhang, W. Yi, et al, Thermo-mechanical design of the neutralizer for CRAFT negative ion-based neutral beam injection system. Fusion Eng. Des. **169**, 112482 (2021). doi: 10.1016/j.fusengdes.2021.11248

[45] W. Yi, J.L. Wei, Y.M. Gu, et al., Final design and manufacturing of the neutralizer for the negative ion-based neutral beam injector test facility of CRAFT. Fusion Eng. Des. **194**, 113749 (2023). doi: 10.1016/j.fusengdes.2023.113749

[46] L.Z. Liang, C. Li, X.L. Wang, et al., Preliminary thermal hydraulic analyses on electrostatic residual ion dump for CRAFT NNBI. Fusion Eng. Des. **190**, 113499 (2023). doi: 10.1016/j.fusengdes.2023.113499

[47] N. Tang, C.D. Hu, Y.L. Xie, et al., Thermal analysis and optimization of the calorimeter verification prototype of a negative ion-based neutral beam injection system. Fusion Eng. Des. **176**, 113018 (2022). doi: 10.1016/j.fusengdes.2022.113018

[48] L. Tao, Y.L. Xie, C.D. Hu, et al., Design and Verification of Calorimeter for CFETR Neutral Beam Injection System Proto-

type with Negative Ion Source. Fusion Sci. Technol. **78**, 490-502 (2022). doi: 10.1080/15361055.2022.2050131

[49] C.D. Hu, J.Q. Lang, Y.L. Xie, et al., Pumping performance analysis of negative ion based neutral beam injector cryosorption pump prototype. Fusion Eng. Des. **189**, 113469 (2023). doi: 10.1016/j.fusengdes.2023.113469

[50] Q.X. Wang, Y.L. Xie, H.H. Hong, et al., Analysis and optimization of LN2 two-phase flow in CRAFT NNBI cryopump. Nucl. Eng. Technol., (2024). doi: 10.1016/j.net.2024.08.047

[51] Y.M. Gu, J.L. Wei, J.C. Chen, et al., The engineering design of half-size RF negative ion source for CRAFT-NNBI. Fusion Eng. Des. **192**, 113603 (2023). doi: 10.1016/j.fusengdes.2023.113603

[52] J.H. Wang, Y. Wang, Y.W. Yang, et al., Optimization of a large-area grid electrode for negative ion source in fusion neutral beam injector. Nucl. Eng. Technol., (2024). doi: 10.1016/j.net.2024.08.051

[53] Y.L. Yang, Y. Wu, L.Z. Liang, et al., Simulations for the cesium dynamics of the RF-driven prototype ion source for CRAFT N-NBI. Nucl. Eng. Technol. **56**, 1145-1152 (2024). doi: 10.1016/j.net.2023.11.019

[54] X.F. Peng, J.L. Wei, Y.W. Yang, et al., Influence of plasma grid bias on the beam extraction of RF driven negative hydrogen ion source. Phys. Plasmas **30**, 103507 (2023). doi: 10.1063/5.0156271

[55] K. Tsumori, K. Nagaoka, M. Osakabe, et al., High power beam injection using an improved negative on source for the large helical device. Rev. Sci. Instrum. **75**, 1847-1850 (2004). doi: 10.1063/1.1702107

[56] C.F. Barnett, H.T. Hunter, M.I. Fitzpatrick, et al., Collisions of H, H2, He and Li atoms and ions with atoms and molecules. ORNL-6086(1990). doi: 10.2172/6570226

[57] J. Kim, H.H. Haselton. Analysis of particle species evolution in neutral-beam injection lines. J. Appl. Phys. **50**,3802(1979). doi: 10.1063/1.326504

[58] J.L. Wei, C.D. Hu, L.Z. Liang et al., Modeling the gas flow in the neutralizer of ITER neutral beam injector using Direct Simulation Monte Carlo approach. Fusion Eng. Des. **88**, 46-50 (2013). doi: 10.1016/j.fusengdes.2012.10.004

[59] G. Ito, R. Kawashima, K. Komurasaki, et al. Inflow angular dependence of the capture coefficient in cryopumps. Vacuum **160**,102-108 (2019). doi: 10.1016/j.vacuum.2018.11.013

[60] G. Fan, J. R. Manson. Calculations of the energy accommodation coefficient for gas-surface interactions. Chem. Phys. **370**,175-179 (2010). doi: 10.1016/j.chemphys.2009.12.018

[61] X. Luo, C. Day. 3D Monte Carlo vacuum modeling of the neutral beam injection system of ITER, Fusion Eng. Des. **85**, 1446-1450 (2010). doi: 10.1016/j.fusengdes.2010.04.002

[62] L. Rossi, F. Castejón, C. Moreno. Study of plasma formation within the electrostatic residual ion dump proposed for the HNB injectors of ITER. Nucl. Fusion **49**, 015002 (2009). doi: 10.1088/0029-5515/49/1/015002

[63] A. Krylov and R.S. Hemsworth, Gas flow and related beam losses in the ITER neutral beam injector. Fusion Eng. Des. **81**, 2239-2248 (2006). doi: 10.1016/j.fusengdes.2006.03.006

[64] M. Dremel, C. Day, S. Hanke, et al. Cryopump design development for the ITER Neutral Beam Injectors. Fusion Eng. Des. **84**, 689-693 (2009). doi: 10.1016/j.fusengdes.2009.01.004

[65] X. Li, Y. J. Xu, L. Yu, et al. Analysis of Power Distribution on Beamline Components at Different Neutralization Efficiencies on NBI Test Stand. Plasma Sci. Technol. **18**, 1215 (2016). doi: 10.1088/1009-0630/18/12/12

[66] T.S. Kim, S.R. In, D.H. Chang, et al. Neutralizer experiment of KSTAR NBTS system. Vacuum **84**, 568-572 (2010). doi: 10.1016/j.vacuum.2009.06.052